

Infrared Excess and Molecular Gas in the Galactic Worm GW46.4+5.5

Kee-Tae Kim, Jeong-Eun Lee, and Bon-Chul Koo

Department of Astronomy, Seoul National University, Seoul 151-742, Korea

ABSTRACT

We have carried out high-resolution ($\sim 3'$) HI and CO line observations along one-dimensional cuts through the Galactic worm GW46.4+5.5. By comparing the HI data with *IRAS* data, we have derived the distributions of I_{100} excess and τ_{100} excess, which are respectively the 100 μm intensity and 100 μm optical depth in excess of what would be expected from HI emission. In two observed regions, we were able to make a detailed comparison of the infrared excess and the CO emission. We have found that τ_{100} excess has a very good correlation with the integrated intensity of CO emission, W_{CO} , but I_{100} excess does not. There are two reasons for the poor correlation between I_{100} excess and W_{CO} : firstly, there are regions with enhanced infrared emissivity without CO, and secondly, dust grains associated with molecular gas have a low infrared emissivity. In one region, these two factors completely hide the presence of molecular gas in the infrared. In the second region, we could identify the area with molecular gas, but I_{100} excess significantly underestimates the column density of molecular hydrogen because of the second factor mentioned above. We therefore conclude that τ_{100} excess, rather than I_{100} excess, is an accurate indicator of molecular content along the line of sight. We derive $\tau_{100}/N(\text{H})=(1.00\pm 0.02)\times 10^{-5} (10^{20} \text{ cm}^{-2})^{-1}$, and $X \equiv N(\text{H}_2)/W_{\text{CO}}\simeq 0.7\times 10^{20} \text{ cm}^{-2} (\text{K km s}^{-1})^{-1}$. Our results suggest that I_{100} excess could still be used to estimate the molecular content if the result is multiplied by a correction factor $\xi_c \equiv \langle I_{100}/N(\text{H}) \rangle_{\text{HI}}/\langle I_{100}/N(\text{H}) \rangle_{\text{H}_2}$ ($\simeq 2$ in the second region), which accounts for the different infrared emissivities of atomic and molecular gas. We also discuss some limitations of this work, which could stem from using single-temperature model and the *IRAS* 60 μm intensity in estimating the dust optical depth along the line of sight.

Subject headings: ISM: individual (GW46.4+5.5) — infrared: ISM: continuum — ISM: molecules — radio lines: ISM

1. Introduction

In many studies of the interstellar medium, it is essential to determine accurately the amount of molecular gas along the line of sight. However, the most abundant molecule, H_2 , not only has a large excitation temperature ($T_{\text{ex}} \geq 509$ K), which is not usually attainable in a cold interstellar medium, but also has very small rotational transition probabilities. In order to infer the H_2 column density $N(\text{H}_2)$, therefore, we generally rely on indirect methods. The most well-known indirect method for estimating the H_2 column density is to observe other molecules such as CO, CS, or NH_3 . However, the fractional abundance of a molecule relative to H_2 is unlikely to be uniform from one cloud to another, or even sometimes within a cloud. In addition, there may be some differences among the distributions of individual molecules because of their different photochemical properties. In the case of CO, which has been widely used as a tracer of H_2 , the abundance varies from cloud to cloud by up to three orders of magnitude depending on the visual extinction and astrochemical properties (Scoville & Sanders 1987; van Dishoeck & Black 1988; Magnani & Onello 1995).

The infrared all-sky maps produced by the *Infrared Astronomical Satellite* (*IRAS*) mission presented a new opportunity to study the distribution of interstellar molecular gas. The Galactic radiation in the far-infrared (far-IR) appears to arise mostly from dust grains well-mixed with interstellar gas (Mathis, Mezger, & Panagia 1983). The *IRAS* 100 μm emission intensity, I_{100} , has been found to be tightly correlated with the total column density of interstellar gas at $|b| \geq 5^\circ$, and the 100 μm emissivity per hydrogen nucleus, $I_{100}/N(\text{H})$, seems to be fairly uniform in the solar neighborhood: $I_{100}/N(\text{H}) \simeq 1 \text{ MJy sr}^{-1} (10^{20} \text{ cm}^{-2})^{-1}$ (de Vries et al. 1987; Boulanger & Pérault 1988; Heiles, Reach, & Koo 1988; Deul & Burton 1990, 1992). Therefore, I_{100} excess, i.e., the *IRAS* 100 μm emission in excess of what is expected from the HI column density, could be used as a tracer of H_2 in regions where the amount of ionized gas is negligible. Based on such an idea, several groups have identified “infrared-excess (IR-excess)” clouds in order to investigate the distribution of molecular gas. However CO observational studies on the IR-excess clouds showed that there is a substantial difference between the distribution of IR-excess clouds and that of CO-emitting clouds (Désert,

Bazell, & Boulanger 1988; Blitz, Bazell, & Désert 1990; Heithausen et al. 1993; Reach, Koo, & Heiles 1994; Meyerdierks & Heithausen 1996; Reach, Wall, & Odegard 1998). This discrepancy between the two distributions is in a sense expected, because firstly the dust abundance and radiation-field strength vary, and secondly the CO abundance is low in diffuse molecular clouds, and finally the infrared emissivity of the dust associated with molecular gas is low.

Another *IRAS* method for tracing molecular gas is to use 100 μm optical depth, τ_{100} . This might be more accurate than using 100 μm intensity, at least in principle, because optical depth is simply proportional to the amount of dust along the line of sight if dust properties are the same. Indeed, for several high-latitude clouds, 100 μm (or 60 μm) optical depth has been found to be correlated with molecular gas column density better than the 100 μm intensity alone (Langer et al. 1989; Snell, Heyer, & Schloerb 1989; Jarrett, Dickman, & Herbst 1989). ‘IRAS’ clouds similar to the IR-excess clouds have been identified using this method, too (Wood et al. 1994). These previous studies, which were limited to high latitudes ($|b| \gtrsim 10^\circ$), however, simply calculated dust optical depth after subtracting flat background emission from the 60 and 100 μm intensity maps and showed that it had a very good correlation with the integrated intensities of CO isotopes.

In this paper, we make a detailed comparison of 100 μm intensity, 100 μm optical depth, and the distribution of CO emission along several one-dimensional cuts. Our study differs from most previous studies in that we use both high-resolution ($\sim 3'$) HI and CO data in the analysis (cf. Reach et al. 1994). The HI data make it possible to derive accurate correlations between τ_{100} (or I_{100}) and $N(\text{HI})$, which is used to identify ‘ τ_{100} -excess’ (or I_{100} -excess) regions and to estimate the excess column densities of H nuclei. This excess H column density is compared with the distribution of CO integrated intensity, W_{CO} , to derive the important conversion factor $X \equiv N(\text{H}_2)/W_{\text{CO}}$. For comparison, most previous studies (e.g., de Vries et al. 1987; Heithausen & Thaddeus 1990) that derived the conversion factor from the *IRAS* data have been based on the comparison of I_{100} excess and W_{CO} , which may significantly underestimate X (Magnani & Onello 1995; Reach et al. 1998). In this paper we compare these two approaches in detail and discuss their limitations.

The object that we study in this paper is the

galactic worm GW46.4+5.5. Galactic worms are wiggly, vertical structures which look like worms crawling away from the Galactic plane in median-filtered HI maps (Heiles 1984; Koo, Heiles, & Reach 1992). GW46.4+5.5 is a $\sim 8^\circ$ long, filamentary structure extending vertically from the Galactic plane in both far-IR (or HI) and radio continuum emission (Figure 1). It is possible that GW46.4+5.5 is the wall of a super-shell similar to the North Polar Spur, but at a greater distance (Kim, Koo & Heiles 1999). We describe the HI and CO line observations in Section 2. In Section 3 we evaluate I_{100} and τ_{100} excesses using the *IRAS* and HI data, and compare their distributions with that of W_{CO} . We discuss the nature of I_{100} excess in GW46.4+5.5 and some potential problems of τ_{100} -excess method in Section 4. The main conclusions are summarized in Section 5.

2. Observations

HI 21 cm line observations were carried out using the 305 m telescope at Arecibo Observatory in 1990 October. The telescope had a HPBW of $3.3'$ and a beam efficiency of 0.8 at 1.4 GHz (Reach, Koo, & Heiles 1994). We observed both circular polarizations simultaneously using two 1024 channel correlators with 5 MHz bandwidth each, so that the velocity resolution was 2.03 km s^{-1} after Hanning smoothing. Each spectrum was obtained by integrating for 1 minute using frequency switching. We made a total of 9 one-dimensional cuts through GW46.4+5.5 at a set of constant galactic latitudes. The beam separation was $3'$. The positions of our one-dimensional cuts are listed in Table 1.

CO J=1–0 line observations were made in 1994 February using the 4 m telescope (HPBW= $2.5'$) at Nagoya University in Japan. We obtained 8 one-dimensional cuts in the same way as in the HI line observations. The observed positions together with their reference positions are summarized in Table 1. An SIS mixer receiver and a 1664 channel Acousto-Optical Spectrometer (AOS) with 40 MHz bandwidth were used. The velocity resolution was 0.67 km s^{-1} after Gaussian smoothing. The system temperature varied in the range 480–700 K during the observing sessions depending on weather conditions and elevation of the source. Absolute-position switching instead of frequency switching was used in order to prevent the contamination of spectra by the atmospheric CO emission. The reference positions were checked to

be free of appreciable ($T_{\text{R}}^* < 0.1 \text{ K}$) CO emission. The velocity was centered at $v_{\text{LSR}} = 40 \text{ km s}^{-1}$ and the velocity coverage was from -19 to $+91 \text{ km s}^{-1}$. The on-source integration time was 2 minutes and the typical rms noise level was 0.2 K per channel after Gaussian smoothing. The intensity scale was calibrated with respect to the standard source S140 which was assumed to have $T_{\text{R}}^* = 20 \text{ K}$ (Yang & Fukui 1992).

3. Infrared Excess and Molecular Gas

3.1. HI Gas and Infrared Excess

Figure 2 shows a sample from our HI spectrum at $(l, b) = (45.^\circ 10, 4.^\circ 00)$ where the strongest CO line emission was detected. There are three peaks at positive velocities in the HI spectrum and the peaks in the velocity range $v_{\text{LSR}} \simeq 18\text{--}40 \text{ km s}^{-1}$ are the components associated with GW46.4+5.5 (Kim et al. 1999). The components at negative velocities might be from the warped Galactic plane outside of the solar circle. The physical and dynamical properties of the worm will be discussed in a separate paper (Kim et al. 1999).

We assume that the HI emission is optically thin and compute the HI column density along a given line of sight, $N(\text{HI})$, from

$$N(\text{HI}) = 1.822 \times 10^{18} \int T_{\text{b}} dv \quad \text{cm}^{-2}, \quad (1)$$

where T_{b} is the brightness temperature in K and v is the velocity in km s^{-1} . Our assumption seems to be valid because the peak temperature of the HI line is much lower than the typical spin temperature of HI gas, $T_{\text{s}} = 125 \text{ K}$, for most sight lines. The integral range is from $v_{\text{LSR}} = -100$ to $+150 \text{ km s}^{-1}$. Figure 3a is the plot of the $100 \mu\text{m}$ intensity, I_{100} , against $N(\text{HI})$ in the observed regions. We can see a strong correlation between the two physical parameters. Different beam sizes of the HI and *IRAS* observations could introduce some scattered data points in the figure. But the effect must be small because the beam sizes are roughly the same ($\sim 3'$). The figure shows only the data from the regions at $b \geq 3^\circ$ where both HI and CO line observations were made. The data at lower galactic latitudes are not used because of the possible contribution from dust associated with ionized gas. The open circles, squares, and pentagons represent the points with detectable CO emission at $b = 3^\circ, 4^\circ, \text{ and } 5^\circ$, respectively. The area of each

symbol is proportional to the integrated CO intensity. The crosses represent the points without detectable CO. A least-squares fit excluding the points with detectable CO yields $(I_{100}/\text{MJy sr}^{-1}) = (1.32 \pm 0.02)$ $(N(\text{HI})/10^{20} \text{ cm}^{-2}) - 3.37 \pm 0.7$. Our fitting procedure involves two steps: (1) All the crosses are fitted to a straight line, and (2) the crosses within $\pm 2\sigma$ deviation from the first fit are fitted to a new straight line. The negative zero-intercept could be from errors in the subtraction of zodiacal light. The derived $I_{100}/N(\text{HI})$ agrees with the results of previous observational studies. For example, Boulanger et al. (1986), de Vries et al (1987), and Heiles et al. (1988) obtained 1.4 ± 0.3 , 1.0 ± 0.4 , and ~ 1.3 $\text{MJy sr}^{-1} (10^{20} \text{ cm}^{-2})^{-1}$, respectively.

We now compare the HI column density and 100 μm optical depth. Assuming that the far-IR emission is optically thin and that the temperature of dust grains is constant along the line of sight, the 60/100 μm color temperature, T_d , can be derived according to the formula

$$T_d = c_1 \left[\frac{1}{\lambda_{60}} - \frac{1}{\lambda_{100}} \right] / \ln \left[\frac{I_{100}}{I_{60}} \left(\frac{\lambda_{100}}{\lambda_{60}} \right)^{n+3} \right], \quad (2)$$

where $c_1 = hc/k_B = 1.441$ and n is the index in the emissivity law, $Q_{\text{abs}}(\lambda) \sim \lambda^{-n}$. For the graphite-silicate dust grain model of Mathis, Rumpl, & Norsdieck (1977; hereafter MRN dust model), n lies between 1 and 2 (Draine & Lee 1984). We take $n=1.5$ in this paper. The 100 μm optical depth, τ_{100} , is derived from $\tau_{100} = I_{100}/B_\lambda(T_d)$, where $B_\lambda(T)$ is the Planck function. Figure 3b displays the 100 μm optical depth versus the HI column density. A strong correlation also exists between these two quantities. A least-squares fit has been performed in a similar way to yield $(\tau_{100}/10^{-5}) = (1.00 \pm 0.02) (N(\text{HI})/10^{20} \text{ cm}^{-2}) + 0.01 \pm 0.6$. The estimated $\tau_{100}/N(\text{H})$ ratio is much smaller than the value $\langle \tau_{100}/N(\text{H}) \rangle = 6.3 \times 10^{-5} (10^{20} \text{ cm}^{-2})^{-1}$ obtained by Boulanger et al. (1996) from an analysis of the *Cosmic Background Explorer (COBE)* mission and the Leiden-Dwingeloo HI survey data. This difference between the two values cannot be entirely due to the calibration difference between the *IRAS* and *COBE* observations. Instead, the difference may be attributed to the effects of small, transiently heated dust grains (Langer et al. 1989) and to the insensitivity of the *IRAS* observations to cold ($T_d < 15$ K) dust grains (Snell et al. 1989; Jarrett et al. 1989; Wood et al. 1994).

If the dust-to-gas ratio and the infrared emissivity per hydrogen nucleus are uniform over the atomic and molecular regions, the infrared excess can be used to estimate the H_2 column density. The infrared excess may be determined either from I_{100} or τ_{100} using the following formulae:

$$N(\text{H}_2)_{I_{100}} \equiv \frac{1}{2} \left[\frac{I_{100,c}}{\langle I_{100,c}/N(\text{H}) \rangle} - N(\text{HI}) \right] \text{ cm}^{-2} \quad (3)$$

and

$$N(\text{H}_2)_{\tau_{100}} \equiv \frac{1}{2} \left[\frac{\tau_{100,c}}{\langle \tau_{100,c}/N(\text{H}) \rangle} - N(\text{HI}) \right] \text{ cm}^{-2}, \quad (4)$$

where the subscript ‘c’ indicates the quantity corrected for offset and the angle bracket indicates an average ratio. Since we excluded the data points with detectable CO, we may use the derived ratios as the ratios with respect to the column density of *hydrogen nuclei*, i.e., $\langle I_{100}/N(\text{H}) \rangle = 1.32$ $\text{MJy sr}^{-1} (10^{20} \text{ cm}^{-2})^{-1}$ and $\langle \tau_{100}/N(\text{H}) \rangle = 1.00 \times 10^{-5} (10^{20} \text{ cm}^{-2})^{-1}$, respectively.

3.2. Comparison of Infrared Excess and CO Line Intensity

We have detected CO emission in five regions (Table 2). Figure 2 shows the spectrum of the strongest CO line and compares it with the corresponding HI spectrum. Note that the velocity range of our CO observations was from -19 to $+91$ km s^{-1} , so that we could not detect the CO emission, if any, associated with the HI gas at negative velocities. It is, however, very unlikely that there is appreciable CO emission in this outer part of the Galaxy. We, in fact, made some test observations with enough velocity coverage, but could not detect any emission ($T_R^* < 0.2$ K). In any case, we believe that we have detected the emission from most of the CO gas. The CO emission from regions C and D is almost certainly associated with GW46.4+5.5, while that from regions A and B is probably not because the velocities are very different. The CO emission from region E is also possibly related to the worm although its central velocity is somewhat lower than the velocity of the worm. The physical association of molecular gas with GW46.4+5.5 will be discussed in a separate paper (Kim et al. 1999). As we have mentioned in

Section 3.1, the regions at $b=1^\circ$ (A and B) are not included in our analysis because of the complication due to the presence of ionized gas. Region E is not included because it has only a few observed points. We thus limit our subsequent analysis to regions C and D.

Figures 4a and 4b compare the values of $N(\text{H}_2)$ derived from equations (3) and (4) with the integrated CO line intensity in regions C and D, respectively. The integral ranges are from $v_{\text{LSR}}=+20$ to $+40$ km s^{-1} for region C and from $v_{\text{LSR}}=+15$ to $+30$ km s^{-1} for region D. These are velocity ranges where the CO emission is detected. In region C, the $N(\text{H}_2)_{\tau_{100}}$ distribution matches very well that of W_{CO} , but the $N(\text{H}_2)_{I_{100}}$ distribution does *not*. The $N(\text{H}_2)_{I_{100}}$ distribution differs from that of W_{CO} significantly at $b \simeq 46^\circ - 47^\circ$. In region D, on the other hand, both $N(\text{H}_2)_{\tau_{100}}$ and $N(\text{H}_2)_{I_{100}}$ match very well with W_{CO} although their absolute scales differ by about a factor of 2. Hence, τ_{100} excess appears to trace molecular gas better than I_{100} excess, which is also obvious from Figures 3a and 3b since the points with CO are separated more clearly from those without CO in the latter. This is more clearly shown in Figure 5, where $N(\text{H}_2)_{\tau_{100}}$ and $N(\text{H}_2)_{I_{100}}$ are compared with W_{CO} . $N(\text{H}_2)_{\tau_{100}}$ is obviously proportional to W_{CO} whereas $N(\text{H}_2)_{I_{100}}$ has much weaker correlation with W_{CO} . We determined $N(\text{H}_2)_{\tau_{100}}/W_{\text{CO}} = (0.70 \pm 0.05) \times 10^{20} \text{ cm}^{-2} (\text{K km s}^{-1})^{-1}$ by a least-squares fit. The error quoted represents only a statistical error in the fit. This conversion factor is much smaller than the estimated value for molecular clouds in the Galactic plane, $X = (1.8 - 4.8) \times 10^{20} \text{ cm}^{-2} (\text{K km s}^{-1})^{-1}$ (Scoville & Sanders 1987), but comparable to that of high latitude clouds, $X \simeq 0.5 \times 10^{20} \text{ cm}^{-2} (\text{K km s}^{-1})^{-1}$ (e.g., de Vries et al. 1987; Heithausen & Thaddeus 1990; Reach et al. 1998). Since there seems to be a systematic difference between the correlations in regions C and D, we also determined the slopes of the correlations separately. They are (0.40 ± 0.05) and $(0.93 \pm 0.06) \times 10^{20} \text{ cm}^{-2} (\text{K km s}^{-1})^{-1}$, respectively. This difference could be due to variations in the dust-to-gas ratio (Magnani & Onello 1995) or due to variations of the gas-phase carbon abundance (Heithausen & Mebold 1989). Further study is needed to address this question.

As we will discuss in more detail in Section 4.2, the correlation between W_{CO} and $N(\text{H}_2)_{I_{100}}$ is not apparent partly because of the existence of a local

heating source in region C. If we limit the analysis to region D, there is a weak correlation between the two quantities, $N(\text{H}_2)_{I_{100}}/W_{\text{CO}} = (0.59 \pm 0.05) \times 10^{20} \text{ cm}^{-2} (\text{K km s}^{-1})^{-1}$. Note that the coefficient of proportionality is about 1/2 that of the $W_{\text{CO}}-N(\text{H}_2)_{\tau_{100}}$ relationship, the significance of which will be discussed in next section.

4. Discussions

4.1. IR excess as a Molecular Tracer

4.1.1 I_{100} excess as a molecular tracer

We have found that the I_{100} -excess distribution does not correlate well with the CO distribution. The discrepancy between the two distributions has also been noted in several previous studies (Désert et al. 1988; Blitz et al. 1990; Heithausen et al. 1993; Reach et al. 1994; Meyerdierks & Heithausen 1996; Reach et al. 1998). In general, the regions with such discrepancies are divided into two categories: (a) I_{100} -excess regions without CO emission, and (b) CO-emitting regions without I_{100} excess. The sources that fall into the first category could be regions with enhanced $100 \mu\text{m}$ emissivity. The $100 \mu\text{m}$ emissivity is generally dependent on the dust-to-gas ratio and dust temperature. It has been found that the dust-to-gas ratio changes with position on an angular scale of $\sim 10^\circ$ and by up to a factor of 4 (Burstein & Heiles 1978; Désert et al. 1988). Variation in the dust-to-gas ratios on smaller scales is expected, too. The steady-state temperature of dust grains is determined by their optical properties and the intensity of radiation field (e.g., Draine & Anderson 1985). The I_{100} -excess region at $l \simeq 46^\circ$ in region C is due to the strong radiation field from a nearby O star (see Section 4.2). Alternatively, the sources could be diffuse molecular clouds without detectable CO (Blitz et al. 1990; Reach et al. 1994; Meyerdierks & Heithausen 1996; Reach et al. 1998). This is possible because CO may not be shielded by HI, H_2 , and dust from photodissociation, and is unlikely to be collisionally excited in the low-density region. On the other hand, the sources in the second category, i.e., molecular clouds without I_{100} excess, could be present because of the low emissivity of dust grains associated with molecular gas. If there were no embedded heating source in the molecular cloud, the dust temperature drops from the surface to the center of the cloud. According to Mathis et al. (1983), for example, the dust temperature drops by about 3 K from the edge to the center for a cloud with

$A_v=5$ mag. The 100 μm emissivity of dust grains is very sensitive to dust temperature and changes by about 40% as dust temperature changes by 1 K over the range $18 \leq T_d \leq 25$ K. At $l \simeq 46^\circ 3$ in region C, the low emissivity almost completely counterbalances the significant fraction of I_{100} excess from dust grains associated with molecular gas.

The low far-IR emissivity of molecular clouds has another important implication for using I_{100} excess as a molecular tracer. *The I_{100} excess significantly underestimates the H_2 column density.* In region D, the H_2 column density derived from I_{100} excess is smaller than that derived from τ_{100} excess by about a factor of 2. This is because in equation (3) we used $\langle I_{100}/N(\text{H}) \rangle$ obtained from HI line observations. If there is a molecular cloud along the line of sight, a correct expression for the observed 100 μm emission would be

$$I_{100} = \langle I_{100}/N(\text{H}) \rangle_{\text{HI}} N(\text{HI}) + 2 \langle I_{100}/N(\text{H}) \rangle_{\text{H}_2} N(\text{H}_2), \quad (5)$$

where $\langle I_{100}/N(\text{H}) \rangle_{\text{HI}}$ and $\langle I_{100}/N(\text{H}) \rangle_{\text{H}_2}$ are, respectively, 100 μm emissivities per hydrogen nucleus in atomic and molecular regions. Hence, we need to apply a correction factor ξ_c to $N(\text{H}_2)_{I_{100}}$ in equation (3) in order to obtain an accurate H_2 column density:

$$\xi_c \equiv \langle I_{100}/N(\text{H}) \rangle_{\text{HI}} / \langle I_{100}/N(\text{H}) \rangle_{\text{H}_2}. \quad (6)$$

Since $\langle I_{100}/N(\text{H}) \rangle_{\text{HI}}$ is in general greater than $\langle I_{100}/N(\text{H}) \rangle_{\text{H}_2}$, $\xi_c \geq 1$ and, in GW46.4+5.5, $\xi_c \simeq 2$. Our correction factor ξ_c is equivalent to $\langle B_\nu(T_d) \rangle_{\text{HI}} / \langle B_\nu(T_d) \rangle_{\text{H}_2}$ used by Magnani & Onello (1995) and Reach et al. (1998). From their study of I_{100} -excess clouds, Reach et al. (1998), for example, found $\xi_c=3.8$ as an average value for the solar neighborhood. For the inner Galaxy, if we use the mean temperature of $\langle T_d \rangle_{\text{HI}}=21.0 \pm 1.0$ K and $\langle T_d \rangle_{\text{H}_2}=19.0 \pm 1.0$ K derived by Sodroski et al. (1994) using the Diffuse Infrared Background Experiment (DIRBE) 140 and 240 μm observations, we obtain $\xi_c=2.1$. Our result for ξ_c , however, cannot be compared directly with these results because our study is based on the *IRAS* 60 μm brightness which is largely affected by the emission from small grains. Since $B_\nu(T_d)$ is very sensitive to T_d , it is necessary to estimate the correction factor independently in studying specific regions (Lee, Kim, & Koo 1999).

4.1.2 τ_{100} excess as a molecular tracer

According to our results, τ_{100} excess appears to be an accurate indicator of the molecular content along the line of sight; it not only traces the presence of molecular gas correctly but also increases linearly with the amount of molecular gas. There are two reasons for this. First it separates the intensity peaks produced by enhanced infrared emissivity. Second it corrects for the low infrared emissivity of molecular clouds. In the present work, however, there are two limitations as discussed below.

The first limitation stems from using a mean temperature in deriving τ_{100} along the line of sight. The expression for $N(\text{H}_2)$ in equation (4) is, in fact, an exact one if dust properties and the dust-to-gas ratio remain the same in atomic and molecular regions. In practice, however, there is an error because, in deriving τ_{100} on the right hand side of equation (4), we have used an average color temperature along the line of sight (defined in equation (2)) even if we need to use different color temperatures in deriving the optical depths of atomic and molecular regions. It is straightforward to estimate the error when there are only two dust components with different emissivities along the line of sight. If there is atomic gas of optical depth $\tau_{100}(\text{HI})$ at color temperature T_{HI} and molecular gas of optical depth $\tau_{100}(\text{H}_2)$ at $T_{\text{H}_2} (< T_{\text{HI}})$, the ratio of the optical depth τ'_{100} , derived by using a mean color temperature, to the true optical depth τ_{100} is given by

$$\frac{\tau'_{100}}{\tau_{100}} = \left[\frac{1 + r \exp(-\Delta t)}{1 + r \exp(-\frac{\Delta t}{\lambda_{60}/\lambda_{100}})} \right]^{\frac{\lambda_{60}/\lambda_{100}}{1 - \lambda_{60}/\lambda_{100}}} \frac{1 + r \exp(-\Delta t)}{1 + r}, \quad (7)$$

where $r \equiv \tau_{100}(\text{H}_2)/\tau_{100}(\text{HI})$, $\Delta t \equiv (c_1/\lambda_{100})(1/T_{\text{H}_2} - 1/T_{\text{HI}})$, and the other parameters have the same meaning as in Section 3. The derived optical depth is always less than the true value and, as expected, the difference converges to zero as r approaches zero or infinity. Figure 6 shows, as solid lines, how τ'_{100}/τ_{100} varies in the $(r, \Delta t)$ plane. The ratio τ'_{100}/τ_{100} is affected more strongly by the warmer dust associated with atomic gas in the sense that the error in optical depth is larger at $\tau_{100}(\text{H}_2)/\tau_{100}(\text{HI})=r_o (>1)$ than that at $\tau_{100}(\text{H}_2)/\tau_{100}(\text{HI})=1/r_o$ for a given value of Δt . Similar figures can be found in Langer et al. (1989) and Snell et al. (1989), but Figure 6 is a generalized one. The error in optical depth would induce an error in $N(\text{H}_2)_{\tau_{100}}$. The error can be determined

by the following formula:

$$\frac{N(\text{H}_2)_{\tau'_{100}}}{N(\text{H}_2)_{\tau_{100}}} = \frac{\tau'_{100}/\tau_{100} - 1/(1+r)}{r/(1+r)}. \quad (8)$$

The dependence of $N(\text{H}_2)_{\tau'_{100}}/N(\text{H}_2)_{\tau_{100}}$ on $(r, \Delta t)$ is displayed by dotted lines in Figure 6. The ratio $N(\text{H}_2)_{\tau'_{100}}/N(\text{H}_2)_{\tau_{100}}$ is in general smaller than τ'_{100}/τ_{100} for a given $(r, \Delta t)$ pair. The most striking difference between the two quantities is that, as r approaches zero, the error in $N(\text{H}_2)_{\tau_{100}}$ remains constant for given Δt whereas that in τ_{100} tends to zero. Since the visual extinction is $A_V \simeq 1.5$ mag at the CO peak in region D using $N(\text{H})/A_V = 1.9 \times 10^{21} \text{ cm}^{-21} \text{ mag}^{-1}$ (Bohlin, Savage, & Drake 1978), T_{H_2} is expected to be < 3 K lower than T_{HI} (Mathis et al. 1983). Therefore, the error in $N(\text{H}_2)_{\tau_{100}}$ may be $\lesssim 20\%$ in region D where $\tau_{100}(\text{H}_2)/\tau_{100}(\text{HI}) \simeq 1/2$ (See Figure 6). The error in the correction factor ξ_c is directly related to that in $N(\text{H}_2)_{\tau_{100}}$ because it is actually derived from $N(\text{H}_2)_{\tau'_{100}}/N(\text{H}_2)_{I_{100}}: \xi'_c/\xi_c = N(\text{H}_2)_{\tau'_{100}}/N(\text{H}_2)_{\tau_{100}}$.

The second limitation derives from using I_{60} in estimating the dust optical depth. Interstellar dust grains are known to be composed of small, transiently heated grains and classical, large grains in thermal equilibrium (Draine & Anderson 1985; Désert, Boulanger, & Puget 1990). The emission at $60 \mu\text{m}$ comes from both small grains and large grains, while the emission at $100 \mu\text{m}$ originates mainly from large grains. Désert et al. (1990) divided dust grains into three components: Polycyclic Aromatic Hydrocarbons (PAHs), Very Small Grains (VSGs), and Big Grains (BGs). In their model, the contributions of VSGs are $\sim 60\%$ at $60 \mu\text{m}$ and $\sim 15\%$ at $100 \mu\text{m}$ for the solar neighborhood. Sodroski et al. (1994) found from an analysis of the DIRBE and IRAS data that the average values of the contribution of small grains at $60 \mu\text{m}$ are $\sim 40\%$ and $\sim 60\%$ in the inner and outer Galaxy, respectively. IRAS studies of nearby molecular clouds suggest that the small grains are present largely in the halo surrounding the clouds and that their relative abundances vary (Boulanger et al. 1990; Laureijs, Clark, & Prusti 1991; Bernard, Boulanger, Puget 1993). Therefore, τ_{100} that we have derived using I_{60}/I_{100} does *not* represent the usual “optical depth” of dust grains. Instead it might be largely affected by small grains with varying abundances. However, the fact that we do observe a very good correlation between τ_{100} excess and W_{CO} (or τ_{100} and $N(\text{HI})$) seems to indicate that τ_{100} is still proportional to the amount of dust along the line of sight. Compared

to I_{100} , τ_{100} can be interpreted as a quantity corrected for variation in the abundance of small grains as well as variation in the temperature of large grains. If one uses far-IR data at wavelengths longer than $100 \mu\text{m}$, such as the DIRBE data for the 100, 140, and $240 \mu\text{m}$ wavebands, one can resolve this problem. In the present days, however, the IRAS data have the highest angular resolution among the available infrared survey data.

In the past decade, several groups have found for high-latitude clouds that τ_{100} (or τ_{60}) is better correlated with the gas column density than I_{100} (Langer et al. 1989; Snell et al. 1989; Jarrett et al. 1989; Wood et al. 1994). At high latitudes, however, it is unlikely that the τ_{100} -excess distribution is markedly different from the I_{100} -excess distribution, because most high-latitude clouds are diffuse and quiescent compared to the molecular clouds near the Galactic plane. In addition, the low signal-to-noise ratio of I_{60} could introduce a large error in τ_{100} . At low latitudes, on the contrary, the τ_{100} -excess distribution is expected to represent the distribution of molecular gas much better than the I_{100} -excess distribution, because the number density of luminous stars increases and most molecular clouds contain high-extinction regions and/or embedded luminous stars.

4.2. Local Heating Source in GW46.4+5.5

In the case of region C, the I_{100} -excess distribution is largely affected by the variation of dust temperature (Figure 4a). The I_{100} -excess peak at $b=46^\circ$ appears not to be due to dust grains associated with molecular gas but to an increase in dust temperature. We found a massive star, LSII +12°3, near the position of interest, $(l, b) = (46^\circ 0, 3^\circ 0)$ (Drilling 1975). The star was found to be a luminous *blue* giant star, O9 III (Vijapurkar & Drilling 1993). The coordinates of the star are $(\alpha, \beta)_{1950} = (19:03:14.3, 12:46:21)$ or $(l, b) = (45^\circ 97, 2^\circ 75)$. An infrared point source (IRAS19031+1247) and a radio point source with a diffuse extended envelope (Fürst et al. 1990) lie in the vicinity of the star. IRAS19031+1247 seems to be an OH/IR star on the basis of its position in the $(60-25) \mu\text{m}$ versus $(25-12) \mu\text{m}$ color-color diagram (cf. Lewis 1994). In order to reveal the physical relationship between the two sources and the star, further studies are required. We estimate the distance of the massive star to be $d=2.2 \pm 0.8$ kpc, using the spectroscopic data mentioned above and the *UBV* photometric data of Drilling (1975), $V=10^m 72$,

$B - V = 1^m 00$. Here we adopt $M_V = -5^m 3 \pm 0^m 7$ for O9 III (Conti et al. 1983) and $R \equiv A_V / E_{B-V} = 3.3$ because R for the region is likely to be somewhat higher than the average value for the Galactic plane (Turner 1976). The estimated value is barely in agreement with the kinematic distance of HI gas associated with GW46.4+5.5, $d_{\text{kin}} = 1.4$ kpc (Kim et al. 1999).

Figure 7 displays the large-scale distribution of the I_{60}/I_{100} ratio around region C. The I_{60}/I_{100} ratio is enhanced around the massive star, which is located where two arrows meet, and decreases monotonically from the star to the position of interest. Assuming that $Q_{\text{abs}}(\lambda)$ varies as λ^{-n} , the total excess infrared luminosity from the I_{60}/I_{100} enhanced region can be derived from the following formula:

$$L_{\text{IR}}^{\text{ex}} = 4\sigma d^2 \int_{\Omega_s} \left[\langle \tau \rangle_{>T_d} T_d^4 - \langle \tau \rangle_{>T_{d,B}} T_{d,B}^4 \right] d\Omega, \quad (9)$$

where σ is the Stephen-Boltzmann constant, d is the distance to the massive star, and the subscript B indicates quantities in the absence of the star. The Planck-averaged optical depth is defined as $\langle \tau \rangle_{>T} = \int \tau_\lambda B_\lambda(T) d\lambda / \int B_\lambda(T) d\lambda$ ($\propto T_d^{1.5}$ for $n=1.5$). Using $d=2.2$ kpc and $T_{d,B}=25.2$ K ($I_{60}/I_{100}=0.22$ with $n=1.5$), the total excess infrared luminosity is $L_{\text{IR}}^{\text{ex}} = 6500 L_\odot$ over a solid angle of $\Omega_s = 2.4 \times 10^{-4}$ sr. This value is an order of magnitude smaller than the stellar luminosity, $L_* = 2.2 \times 10^5 L_\odot$ (Panagia 1973). Hence, the star has enough luminosity to produce the observed infrared luminosity, and the I_{100} -excess peak at $b=46^\circ 0$ in region C is probably due to heating by an O-type giant star.

5. Conclusions

Infrared (IR) excess, defined as the emission in excess of what would be expected from HI emission, has been used for estimating the amount of molecular gas along the line of sight. However, at the same time, there have been molecular, particularly CO, line studies showing that the method does not necessarily yield reliable results. That is, there are both IR-excess regions without detectable CO and CO-emitting regions without IR excess. Region C in our study is a good example. The sources that fall into the first category could be either regions with enhanced IR emissivity or diffuse molecular clouds without CO emission. In region C, it is excess heating from a nearby O star that produces an IR-excess region. On the other hand,

the sources that fall into the second category could be molecular clouds with low IR emissivity. In region C, the low emissivity completely hides the presence of a molecular cloud in the infrared.

Our result shows that we can avoid the above confusion problem by using the optical-depth excess instead of IR excess, i.e., the optical depth in excess of what would be expected from HI emission. We have found a very good correlation between 100 μm optical-depth (τ_{100}) excess and integrated intensity of CO emission, W_{CO} . We derive the conversion factor between $N(\text{H}_2)$ and W_{CO} , $X \simeq 0.7 \times 10^{20}$ for the galactic worm GW46.4+5.5. According to our result, however, the conversion factors in regions C and D differ by about a factor of 2, although both regions are parts of the worm. A more complete observation is necessary for the study of the variation of the conversion factor.

Another merit of using optical-depth excess, which may be more important, is that it gives an *accurate* value for the amount of molecular gas. IR excess would significantly underestimate $N(\text{H}_2)$ if one uses an IR emissivity estimated from HI emission, $\langle I_{100}/N(\text{H}) \rangle_{\text{HI}}$. We have introduced a correction factor $\xi_c \equiv \langle I_{100}/N(\text{H}) \rangle_{\text{HI}} / \langle I_{100}/N(\text{H}) \rangle_{\text{H}_2}$, which should be applied in order to account for the different IR emissivity of molecular clouds. In general $\xi_c \geq 1$ because dust grains in molecular clouds are usually colder than dust grains in atomic gas. In region D in our study, $\xi_c \simeq 2$. We should therefore be rather cautious in converting IR excess to $N(\text{H}_2)$.

Two potential problems in using optical-depth excess, however, would be the low surface brightness and the contribution of small, transiently heated grains. If the surface brightness is low, the noise and/or the systematic errors produced in the subtraction of zodiacal emission may make it impossible to derive an accurate optical depth. It would be worthwhile to check the applicability of the method at high galactic latitudes. The second problem may be resolved by using far-IR data at wavelengths longer than 100 μm .

We wish to thank Dr. Y. Fukui, Dr. A. Mizuno, and the graduate students of the Department of Physics and Astrophysics, Nagoya University for their help with the CO line observations. We are very grateful to Dr. W. T. Reach and the anonymous referee for their comments and suggestions. We also thank Dr. Hwankyung Sung for helpful discussions, and Mr. Hyo-Ryung Kim for providing some useful CO

line spectra for this work. This work has been supported in part by the 1994 KOSEF International Co-operative Research Fund.

REFERENCES

- Bernard, J. P., Boulanger, F., & Puget, J.-L. 1993, *A&A*, 277, 609
- Blitz, L., Bazell, D., & Désert, F. X. 1990, *ApJ*, 352, L13
- Bohlin, R. C., Savage, B. D., & Drake, J. F. 1978, *ApJS*, 224, 132
- Boulanger, F. et al. 1996, *A&A*, 312, 256
- Boulanger, F., Falgarone, E., Puget, J.-L., & Helou, G. 1990, *ApJ*, 364, 136
- Boulanger, F., & Pérault, M. 1988, *ApJ*, 330, 964
- Burstein, D., & Heiles, C. 1978, 225, 40
- Conti, P., Catharine, D., Garmany, D., De Loore, C., & Vanbeveren, D. 1983, *ApJ*, 274, 302
- de Vries, H. W., Heithausen, A., & Thaddeus, P. 1987, *ApJ*, 319, 723
- Désert, F. X., Bazell, D., & Boulanger, F. 1988, *ApJ*, 334, 815
- Désert, F. X., Boulanger, F., & Puget, J.-L. 1990, *A&A*, 237, 215
- Deul, E. R., & Burton, W. B. 1990, *A&A*, 230, 153
- Deul, E. R., & Burton, W. B. 1992, in *The Galactic Interstellar Medium*, ed. W. B. Burton, B. G. Elmegreen, & R. Genzel (New York: Springer-Verlag), 79
- Draine, B. T., & Anderson, N. 1985, *ApJ*, 292, 494
- Draine, B., T., & Lee, H., M. 1984, *ApJ*, 285, 89
- Drilling, J. S. 1975, *AJ*, 80, 128
- Fürst, E., Reich, W., Reich, P., & Reif, K. 1990, *A&AS*, 85, 805
- Heiles, C., Reach, W. T., & Koo, B.-C. 1988, *ApJ*, 332, 313
- Heithausen, A., & Mebold, U. 1989, *A&A*, 214, 347
- Heithausen, A., Stacy, J. G., de Vries, H. W., Mebold, U. & Thaddeus, P. 1993, *A&A*, 268, 265
- Heithausen, A., & Thaddeus, P. 1990, *ApJ*, 353, L49
- Jarrett, T. H., Dickman, R. L., & Herbst, W. 1989, *ApJ*, 345, 881
- Kim, K.-T., Koo, B.-C., & Heiles, C. 1999, in preparation
- Koo, B.-C., Heiles, C., & Reach, W. T. 1992, *ApJ*, 390, 108
- Langer, W. D., Wilson, R. W., Goldsmith, P. F., & Beichman, C. A. 1989, *ApJ*, 337, 355
- Laureijs, R. J., Clark, F. O., & Prusti, T. 1991, *ApJ*, 372, 185
- Lee, J.-E., Kim, K.-T., & Koo, B.-C. 1999, submitted to *J. Korean Astron. Soc.*
- Lewis, B. M. 1994, *ApJS*, 93, 549
- Magnani, L., Blitz, L., & Mundy, L. 1990, 295, 402 (MBM)
- Magnani, L., & Onello, J. S. 1995, *ApJ*, 443, 169
- Mathis, J. S., Mezger, P. G., & Panagia, N. 1983, *A&A*, 128, 212
- Mathis, J. S., Rumpl, W., & Nordsieck, K., H. 1977, *ApJ*, 217, 425
- Meyerdierks, H., & Heithausen, A. 1996, *A&A*, 313, 929
- Panagia, N. 1973, *ApJ*, 192, 221
- Reach, W. T., Koo, B.-C., & Heiles, C. 1994, 421
- Reach, W. T., Wall, W. F., & Odegard, N. 1998, *ApJ*, 507, 507
- Scoville, N. Z., & Sanders, D. B. 1987, in *Interstellar Processes*, ed. D. Hollenbach, & H. Thronson (Dordrecht: D. Reidel), 21
- Snell, R., Schloerb, F. P., & Heyer, M. H. 1989, *ApJ*, 337, 739
- Sodroski, T. J. et al. 1994, *ApJ*, 428, 638
- Strong, A. W. et al. 1988, *A&A*, 207, 1
- Turner, D. G. 1976, *AJ*, 81, 1125
- van Dishoeck, E. F., & Black, J. H. 1988, *ApJ*, 334, 771
- Vijapurkar, J., & Drilling, J. 1993, *ApJS*, 89, 293
- Wood, D. O. S., Myers, P. C., & Daugherty, D. A. 1994, *ApJS*, 95, 457
- Yang, J., & Fukui, Y. 1992, *ApJ*, 386, 618

This 2-column preprint was prepared with the AAS L^AT_EX macros v4.0.

TABLE 1
POSITIONS OF ONE-DIMENSIONAL CUTS AND OFF POSITIONS

Scan Number	b	l -range		OFFs ^a (l, b)
		HI 21 cm line	CO J=1–0 line	
B1	1.0	42.5–48.0	43.0–45.5	(45.0, 1.5), (43.5, 2.5)
B2	2.0	43.0–45.7	43.0–46.0	(45.0, 1.5), (43.5, 2.5)
B3	3.0	42.5–48.0	44.0–47.0	(43.5, 2.5), (45.8, 4.2)
B4	4.0	43.0–47.5	44.0–46.5	(47.5, 3.5), (45.8, 4.2)
B5	5.0	42.5–50.0	45.0–48.0	(46.5, 5.3), (49.0, 5.5)
B6	6.0	42.5–51.5	46.0–48.5	(46.5, 5.3), (49.0, 5.5)
B7	7.0	42.5–51.5	46.5–47.5	(45.5, 6.5)
B8	8.0	42.5–51.0	46.5–47.5	(48.0, 8.0)
B9	9.0	42.5–51.5

^aOFF positions for CO J=1–0 line observations

TABLE 2
REGIONS WITH CO J=1–0 LINE EMISSION

Region	b	l -range	$v_{\text{LSR}}^{\text{a}}$ (km s ⁻¹)	$T_{\text{R}}^{*\text{a}}$ (K)	$\Delta v_{\text{FWHM}}^{\text{a}}$ (km s ⁻¹)
A	1.0	43.50–43.70	+60	2.5	2.1
B	1.0	44.50–44.75	-10	2.1	2.9
C	3.0	45.30–46.65	+27	3.0	7.8
D	4.0	44.20–45.50	+22	3.3	5.6
E	5.0	47.65–47.95	+14	1.8	2.5

^aLine parameters at peak position

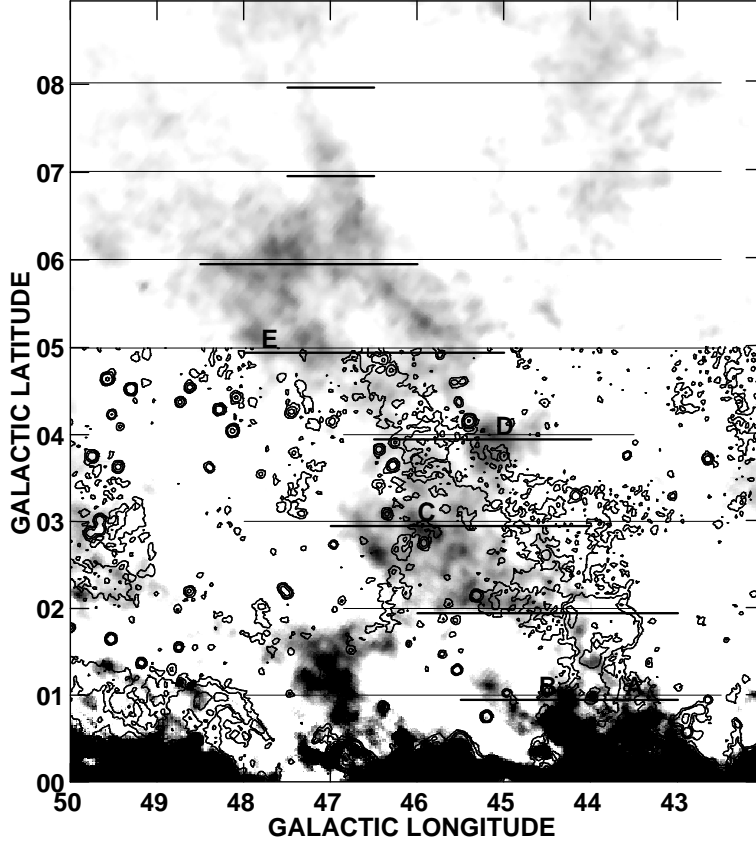


Fig. 1.— $100\ \mu\text{m}$ (grey scale) and 11 cm continuum (contour) images of GW46.4+5.5. The purpose of this figure is to show the morphology of GW46.4+5.5 and to show how the observed regions are related to it. We, therefore, have removed a smooth background emission from the $100\ \mu\text{m}$ and radio continuum maps using a median filter of $6^\circ \times 2^\circ$. GW46.4+5.5 is the far-IR structure extends straight up to $b=7^\circ$ from the Galactic plane. The regions where HI and CO line data were obtained are shown as light and dark solid lines, respectively. For clarity, the dark solid lines are shifted in b -direction from the light ones. The regions with CO line emission are also labeled as A–E. Grey scale intensity range is $1\text{--}30\ \text{MJy sr}^{-1}$. Contour levels are 0.03, 0.1, 0.25, 1.0, and 3 K in brightness temperature.

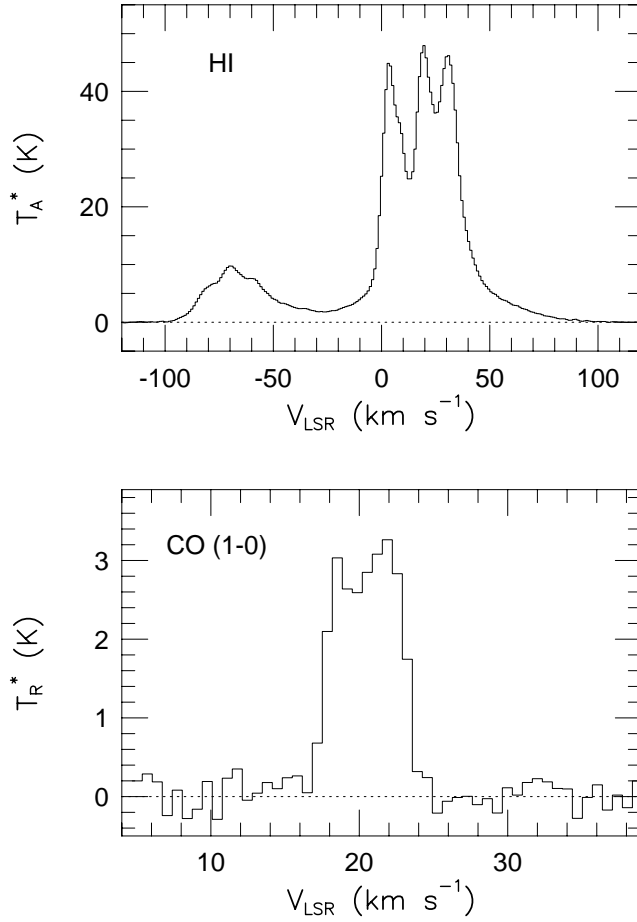


Fig. 2.— HI 21 cm and CO J=1–0 line profiles at $(l, b)=(45^\circ 10, 4^\circ 00)$ where the strongest CO line emission was detected. HI and CO lines were obtained using the Arecibo and Nagoya 4 m telescopes, respectively. The peaks between $v_{\text{LSR}} \simeq 18$ and 40 km s^{-1} in the HI line profile are the components associated with GW46.4+5.5. The peak at $v_{\text{LSR}} \simeq 20 \text{ km s}^{-1}$ has associated molecular gas.

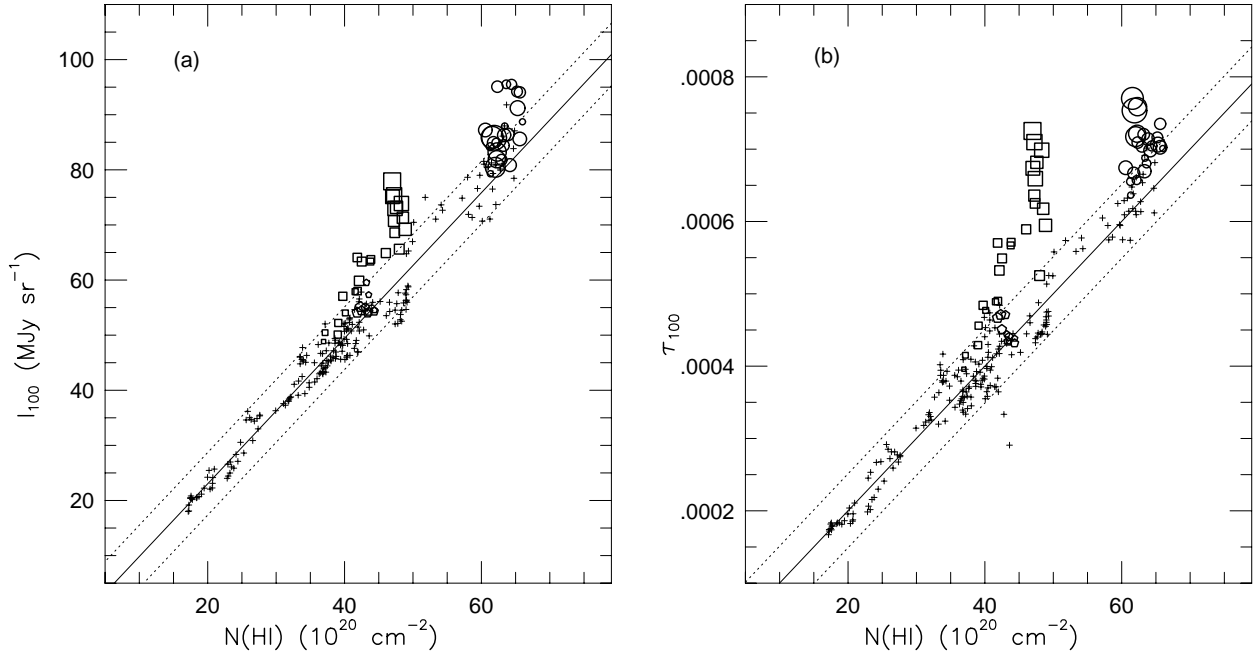


Fig. 3.— (a) I_{100} vs. $N(\text{HI})$ and (b) τ_{100} vs. $N(\text{HI})$. Open circles, squares, and pentagons represent points with detectable CO at $b=3^\circ$, 4° , and 5° , respectively. The area of each symbol is proportional to W_{CO} . Least-squares fits yield $(I_{100}/\text{MJy sr}^{-1}) = 1.32(N(\text{HI})/10^{20} \text{ cm}^{-2}) - 3.37$ and $(\tau_{100}/10^{-5}) = 1.00(N(\text{HI})/10^{20} \text{ cm}^{-2}) + 0.01$, respectively. Results of the fits are shown as solid lines. The dotted lines indicate $\pm 2\sigma$ deviations from the least-squares fit. Note that the points with CO are more clearly separated from the points without CO in (b) than in (a). Also note that the areas of symbols become larger as the points become further away from the fit in (b), whereas they do not in (a).

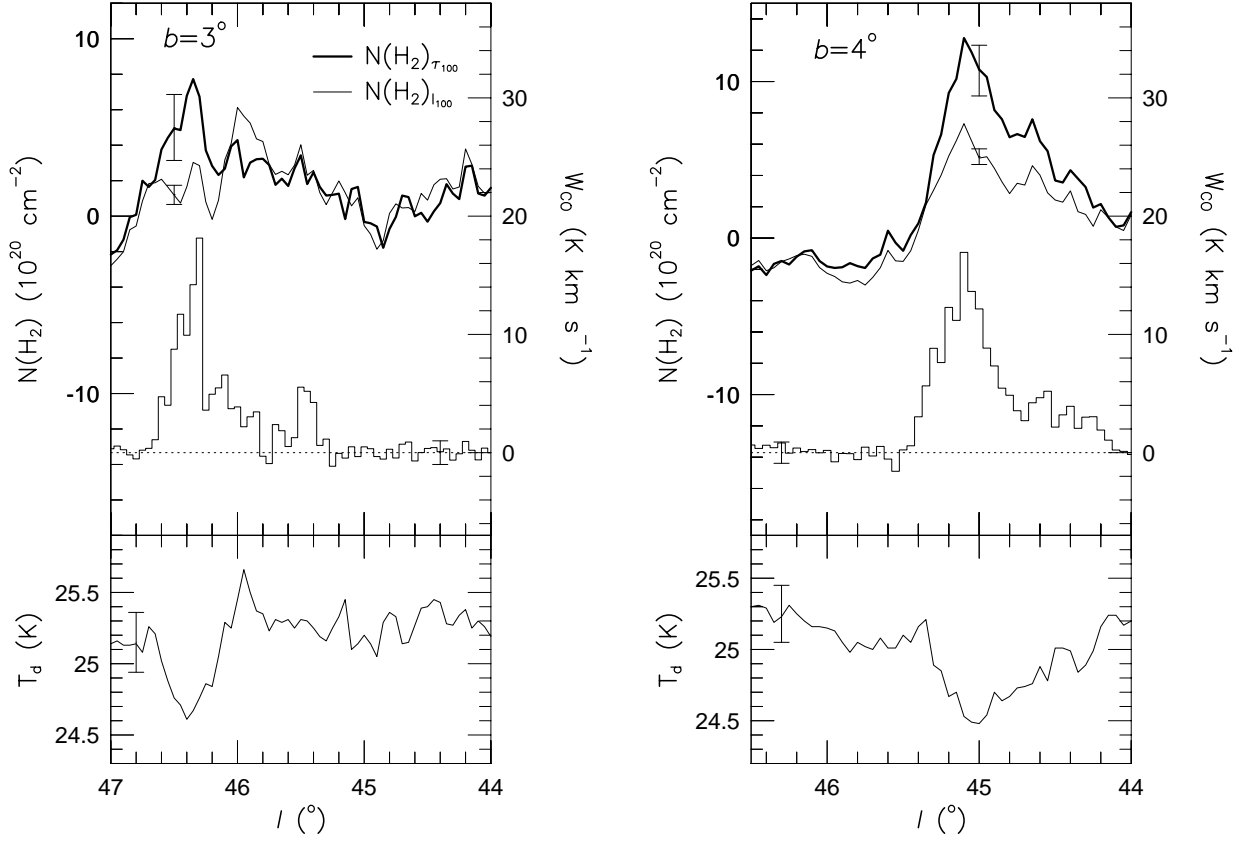


Fig. 4.— Distributions of $N(\text{H}_2)_{I_{100}}$, $N(\text{H}_2)_{\tau_{100}}$, W_{CO} , and T_d at (a) $b=3^\circ$ and (b) $b=4^\circ$. Note that $N(\text{H}_2)_{I_{100}}$ differs considerably from either W_{CO} or $N(\text{H}_2)_{\tau_{100}}$ at $b=3^\circ$. The difference is partly due to a local heating source. It is also noticeable that dust temperature drops in the regions where CO line emission is detected. The typical statistical error bars are given in each panel.

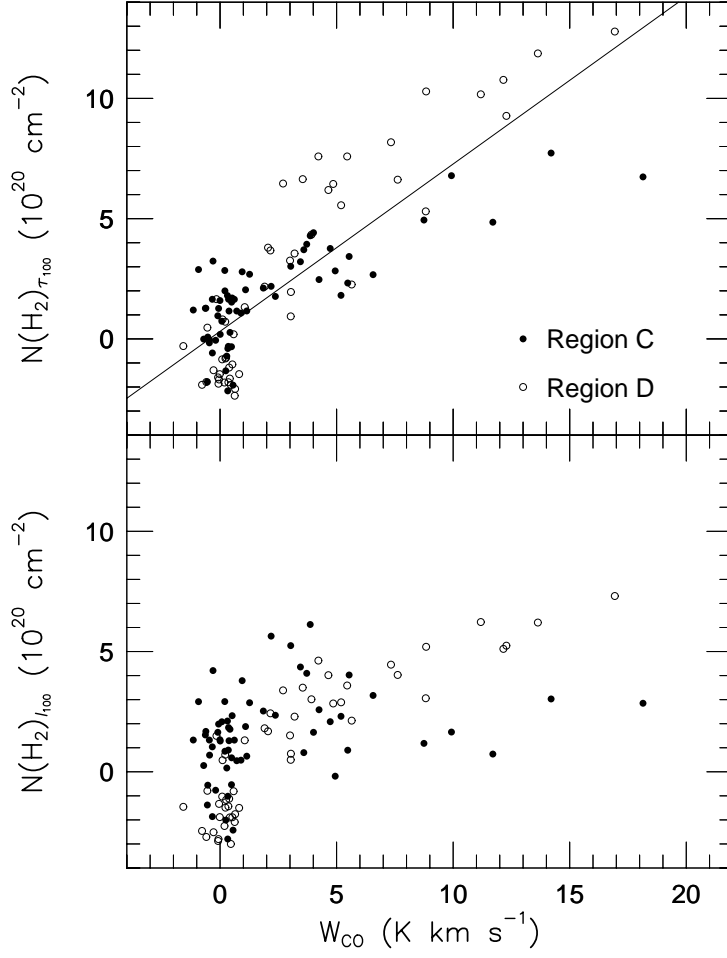


Fig. 5.— Comparison of $N(\text{H}_2)_{\tau_{100}}$ (upper panel) and $N(\text{H}_2)_{I_{100}}$ (lower panel) with W_{CO} . Filled and open circles represent points at $b=3^\circ$ and 4° , respectively. $N(\text{H}_2)_{\tau_{100}}$, but not $N(\text{H}_2)_{I_{100}}$, has a very good correlation with W_{CO} . The straight line is a least-squares fit to the data, $(N(\text{H}_2)_{\tau_{100}}/10^{20} \text{ cm}^{-2}) = 0.70(W_{\text{CO}}/\text{K km s}^{-1}) - 0.31$.

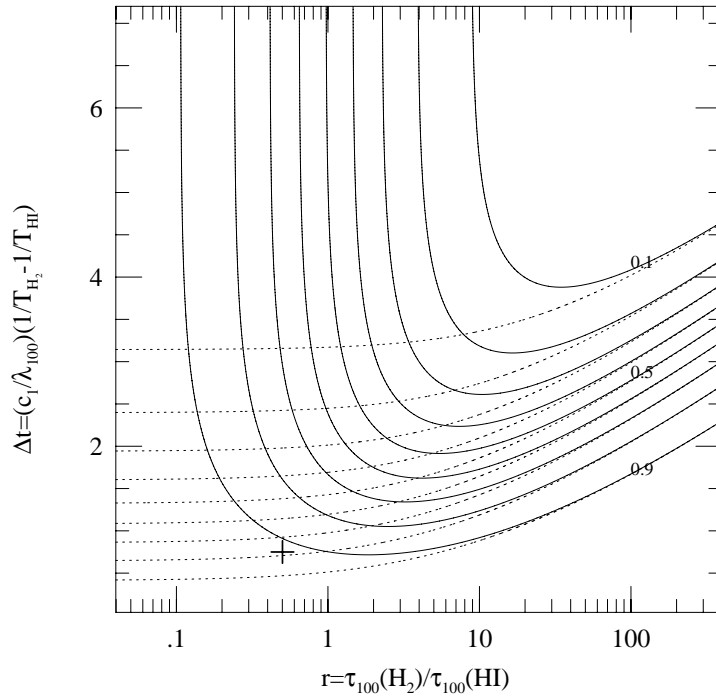


Fig. 6.— Variations of τ'_{100}/τ_{100} (solid line) and $N(\text{H}_2)_{\tau'_{100}}/N(\text{H}_2)_{\tau_{100}}$ (dotted line) in $(r, \Delta t)$ plane. $r \equiv \tau_{100}(\text{H}_2)/\tau_{100}(\text{HI})$ and $\Delta t \equiv (c_1/\lambda_{100})(1/T_{\text{H}_2} - 1/T_{\text{HI}})$, where $c_1/\lambda_{100} = 144$. The τ'_{100}/τ_{100} ratio is weighted toward the warmer dust associated with HI gas, but $N(\text{H}_2)_{\tau'_{100}}/N(\text{H}_2)_{\tau_{100}}$ is not. The difference between the two quantities is larger at smaller r . The cross indicates the position of region D in $(r, \Delta t)$ plane. In order to estimate an upper limit to the error in $N(\text{H}_2)_{\tau_{100}}$ in region D, we assume $(T_{\text{HI}}, T_{\text{H}_2}) = (25.2 \text{ K}, 22.2 \text{ K})$. Contour levels are 0.1, 0.2, ..., 0.9.

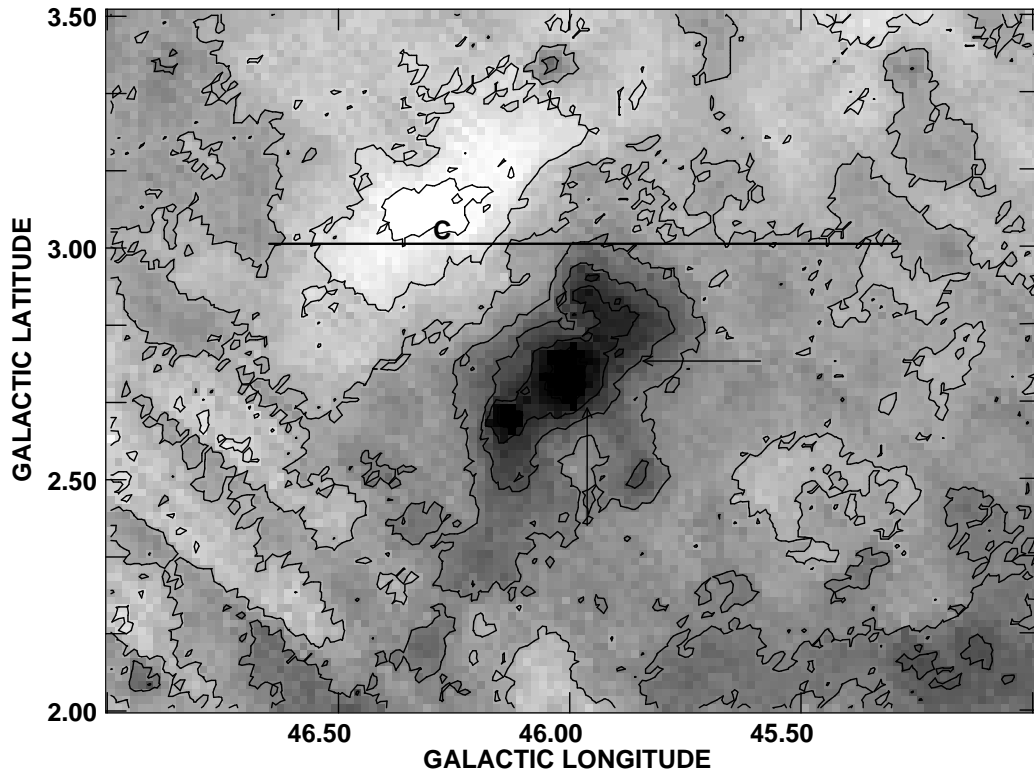


Fig. 7.— Distribution of I_{60}/I_{100} around region C. A luminous blue giant star (LSII+12°3) is located where two arrows meet. Note the high intensity ratio around the star. The region where CO line emission is detected is shown as a solid line. Grey scale intensity range is 0.20–0.26. The lowest contour level is 0.20 and contour spacing is 0.01.